3D Spirals with Controlled Chirality Fabricated Using Metal-Assisted Chemical Etching of Silicon

Owen J. Hildreth,[†,*] Andrei G. Fedorov,[‡,§] and Ching Ping Wong[†,⊥,*]

[†]School of Materials Science and Engineering and [‡]George W. Woodruff School of Mechanical Engineering, Georgia Institute of Technology, 771 Ferst Drive, Atlanta, United States, [§]Parker H. Petit Institute for Bioengineering and Biosciences, Georgia Institute of Technology, 351 Ferst Drive, Atlanta, United States, and [⊥]Department of Electronics Engineering, The Chinese University of Hong Kong, Shitan, Hong Kong, China

ABSTRACT

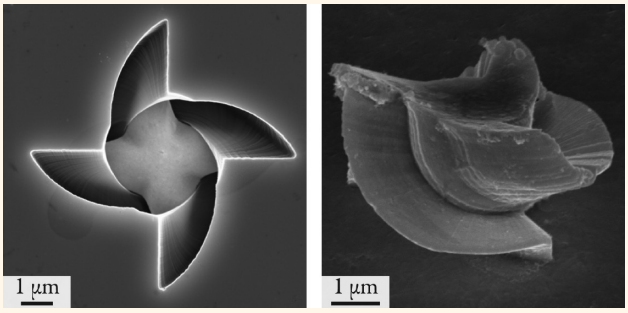

The ability to fabricate 3D spiraling structures using metal-assisted chemical etching (MaCE) is one of the unique advantages of MaCE over traditional etching methods. However, control over the chirality of the spiraling structures has not been established. In this work, a systematic parametric study was undertaken for MaCE of star-shaped catalysts, examining the influence of arm shape, arm length, number of arms, center core diameter, and catalyst thickness on the rotation direction. This data was used to identify a set of geometric parameters that reliably induce rotation in a predefined direction such that large arrays of 3D spiraling structures can be fabricated with the same chirality. Electroless deposition into the MaCE template was used to examine the full etch path of the catalyst and an experimental fit was established to control rotation angle by adjusting the catalyst's center core diameter. The ability to fabricate large arrays of 3D spiraling structures with predefined chirality could have important applications in photonics and optoelectronics.

KEYWORDS: metal-assisted chemical etching · silicon · nanotechnology · etching · 3D · chiral

Fabricating chiral 3D nanostructures with controllable geometry at high volume is difficult. The problem is centered around the fact that the highly refined photolithography and etching processes that enable the large scale fabrication of 2D nanostructures, such as transistors, are inherently a 2D process.[1−8] Specifically, photolithography is limited to taking a 2D pattern and projecting it onto to a 2D surface while standard wet and dry chemical etching processes take a 2D pattern and etch it normally into a wafer or along specific crystallographic directions. While these processes can be combined in creative ways to fabricate complex 2.5D structures,[9] the resulting processing sequences quickly become cumbersome. To this end, a number of alternative techniques are being developed to address these limitations using fundamentally different pattern transfer principles. Some methods, such as X-ray lithography[10,11] or 2-photon lithography,[12,13] focus on moving lithography processes into the third dimension;[2,14] however, these methods still face numerous hurdles before they could be considered mature for industrial applications and more work is needed to improve the cost, feature resolution, and throughput of these processes. Bypassing the issues of 3D lithography are a number of fabrication and etching processes that can create a 3D nanostructure from a standard 2D lithographic pattern. Some of the more interesting of these processes are 3D folding of metallic and composite structures,[15] and metal-assisted chemical etching (MaCE)[16−18] of silicon. These processes take advantage of the high throughput capabilities of standard photolithography and metallization processes, while still providing access to a number of complex 3D structures with useful properties.

MaCE has interesting 3D capabilities. Recent work has shown that MaCE can be used to easily fabricate 3D nanostructures in a single lithography/etch cycle, with example structure including cycloids,[16,19] spirals,[19,20] subsurfaced curved nanohorns,[17] folded pyramids,[18] vertically aligned thin metallic structures,[17,21] spiraling metallic structures, and zigzag nanowires.[22] These 3D capabilities arise because, unlike traditional etching processes that rely on a stationary mask to define the etch profile, the etch profile in

* Address correspondence to cp.wong@mse.gatech.edu, ohildreth@mse.gatech.edu.

Received for review August 13, 2012 and accepted October 4, 2012.

Published online October 04, 2012
10.1021/nn303680k

MaCE is defined by a metal catalyst that travels through 3D space as part of the etch process. In MaCE, a metal catalyst induces a traveling galvanic etching reaction that locally increases the silicon dissolution rate in a solution containing hydrofluoric acid (HF) and an oxidizing agent such as hydrogen peroxide (H_2O_2). The process begins as H_2O_2 is catalytically reduced by the metal particle, which then injects holes (h^+) deep into the valence band of the silicon, creating a hole (h^+)-rich region of silicon (Si*) in the region in immediate contact with the metal. These holes (h^+) are then consumed at the HF/Si* interface in the oxidation of Si^0 to Si^{4+} to produce soluble SiF_6^{2-} and H_2SiF_6,[23] with the etching process continuing as the metal catalyst is driven into the substrate where the silicon around and beneath the catalyst is dissolved.[24−26] Recent reviews on the subject of MaCE are available that provide more information on the effect of etchant composition, catalyst materials and size, dopant levels, and crystallographic orientation, along with applications for MaCE.[27,28]

The 3D capabilities of MaCE are enabled by the fact that the etch profile is defined by a catalyst that travels through 3D space. Work by our group and others has shown that it is possible to control the catalyst travel trajectory by adjusting catalyst shape,[18,19,22,22] introducing pinning structures,[17,21,29] or applying external fields.[30] In our previous work,[19] we showed how spiral structures, such as those exampled in Figure 1, are readily fabricated using a patterned catalyst that has a large central structure to slow the overall etching rate[18] and protrusions that induce a torque about this central structure through the surface−surface interactions between protruding arms and the silicon substrate.[21] While these structures are typically greater than 500 nm, 3D nanostructures are fabricated by patterning holes in the catalyst to create the spiraling coaxial star and radially offset the nanopillars exampled in Figure 1b,c. However, to fabricate spiraling structures for device applications, it is important to establish the protocols necessary to robustly control the chirality of the spiraling catalyst, especially when applied for fabricating the large arrays of nanostructures such as those necessary for chiral-based photonics.

This work seeks to address the issue of controlled chirality. It is accomplished through a parametric study investigating the influence of catalyst shape, feature size, and catalyst thickness on rotation direction. In particular, we demonstrate that catalyst geometry and its deformation during etching, which is geometry-dependent, have a clear influence in controlling chirality. Through the use of electroless deposition we establish a linear relationship between the center core diameter of the catalyst and the final rotation angle. Overall, this study results in a set of MaCE processing conditions to consistently produce spiral etching with predefined chirality and rotation angle.

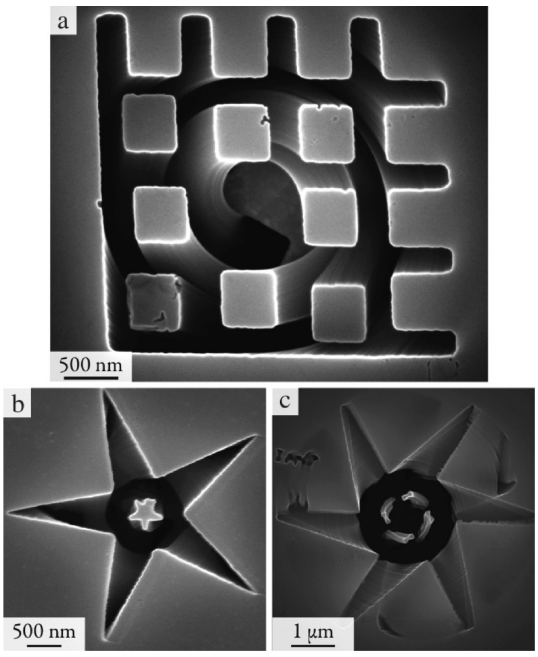

Figure 1. SEM micrographs of example 3D spiraling structures fabricated in silicon using MaCE; (a) grid-shaped pattern where 500 nm square cut-outs in the Au catalyst create 500 nm wide spiraling silicon pillars; (b) star-shaped catalyst where a 350 nm wide triangular cut-out in the middle of the catalyst creates a 350 nm coaxial spiraling triangular pillar; (c) star-shaped catalyst where 100 nm rectangular holes in the catalyst create 100 nm spiraling pillars.

RESULTS AND DISCUSSION

All samples were prepared on p-type, 1−5 Ω-cm, (100) oriented silicon. Initially, 350 nm of polymethyl methacrylate (PMMA) as a positive-tone resist was patterned using a JEOL JBX-9300FS electron beam lithography (EBL) system at 100 kV accelerating voltage and 2 nA beam current with a base dose of 680 μC/cm^2. Four different catalyst stacks of Ti/Au were deposited using electron beam evaporation with measured thicknesses of 51, 64, 79, and 92 nm; the thickness of the Ti layer was kept constant at 15 nm while the Au layer was varied. After lift-off the samples were cleaned using O_2 plasma and then immersed in a stagnant $\rho = 90$[13,8] etchant solution ($HF:H_2O_2:H_2O = 4:1.3:2.8$ mL) for 5 min where $\rho = 100\% \times ([HF]/([HF] + [H_2O_2]))^{x=[HF]}$ is a modified version of the notation established by Chartier *et al.*[23] Note the superscript *x* term was added to designate the dilution of the overall etchant and allows one to easily compare the results of different etchant compositions and dilutions across multiple works. The samples were then imaged using the In-Lens and SE2 detectors of a Zeiss LEO 1550 thermally assisted field emission (TAFE) scanning electron microscope (SEM). After imaging, the 92 nm thick sample was cleaned using O_2 plasma and then ~4 μm of Pd was electrolessly deposited into the MaCE formed templates. A 2 μm thick Au transfer substrate was deposited using electron beam evaporation, and the

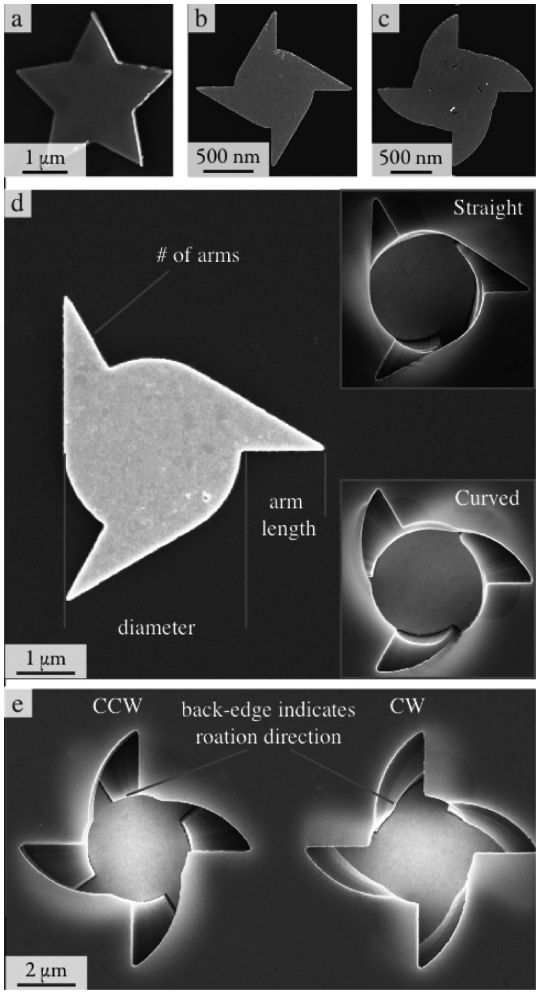

Figure 2. SEM micrographs illustrating the parameters varied to establish the role that catalyst geometry plays in determining catalyst rotation. (a–c) The three catalyst arm shapes tested including symmetric, sawtooth with straight edges, and sawtooth with curved edges. (d) Catalyst geometric variables tested including the number of arms, arm length, center core diameter, and arm shape. The insets show the differences in etch profile between straight versus curved-arm catalysts. (e) Example image showing differences between counter-clockwise (CCW) and clockwise (CW) rotation catalysts as seen from a top-down SEM micrograph.

silicon template was removed using a mixture of 25 wt % of tetramethyl ammonium hydroxide (TMAH) TMAH: H_2O at 80 °C for 24 h.

Star-shaped catalysts were chosen for this study as this geometry readily creates spiraling etching path and also supplies a sufficient number of geometric variables to properly map the parameter space of spiral etching. The SEM micrographs in Figure 2a–d show most of geometric variables tested starting with the overall catalyst shapes of (a) symmetric catalyst arms, (b) asymmetric "sawtooth" catalyst arms with a straight trailing edge, and (c) sawtooth catalyst arms with a curved trailing edge. The number of arms, length of the arms, and center core diameter were also varied as was the overall catalyst thickness. The inset micrographs in Figure 2d illustrate the difference in etch profile between the straight and curved-arm catalysts while Figure 2e illustrates the difference in a counter-clockwise rotation (CCW) *versus* a clockwise (CW) rotation. Note that all the catalysts are oriented such that CCW rotation is toward the shorter, leading edge of the catalyst arms while CW rotation is toward the longer, trailing edge.

Catalyst Arm Shape. he shape of the catalyst arms plays an important role in establishing the catalyst rotation direction. The symmetric stars produced a 50/50 ratio between CCW and CW rotation direction independent of any processing parameters such as catalyst thickness, catalyst top layer (*i.e.*, Ag, Au, Pt, or Pd), etchant composition, or edge lips induced utilizing e-beam shadowing. Changing to the asymmetric sawtooth-shaped catalysts resulted in a dramatic improvement in control over the rotation direction. The graphs in Figure 3 summarize the data of 60 different geometric configurations with 16 catalysts per configuration for each of the 4 different thicknesses (3840 individual catalysts were examined in total). These graphs show the percent of CCW rotation *versus* catalyst geometry parameters such as center core diameter, arm shape (straight = blue circles; curved = red triangles), and catalyst thickness. It is clear that the curved arms show more consistent performance with up to 100% of the curved-arm catalysts rotating in the desired CCW direction, as opposed to the straight-arm catalysts that yields at best around 75% of all rotations in the same direction. There is also a clear dependence on center core diameter and catalyst thickness with control over rotation improved with an increasing core diameter for all but the straight arm, 51 nm thick catalyst shape for which the catalyst arm quickly bent around the center core, thus removing the torque necessary to induce rotation.

Catalyst Thickness, Number of Arms, and Center Core Diameter. Rotation direction is heavily influenced by geometric parameters such as catalyst thickness, number of arms, and arm shape. Catalyst thickness is the easiest parameter to examine, and the effect of this parameter on rotation direction is demonstrated by the SEM micrographs in Figure 4 of 4 × 4 arrays of catalysts with four arms, 4 μm center core diameters, and 2.25 μm arm lengths for the four thicknesses tested. The ratio of CCW rotation *versus* total number of catalysts along with the catalyst thickness is detailed in the top of each SEM micrograph; note that any CW rotations are boxed in black to aid the reader. Examination of these images reveals that the deformation mode of the catalyst changes with thickness: thin catalysts bend with 4-fold symmetry while thicker catalysts transition to 2-fold symmetry. Interestingly, the deformed shape of the catalysts is extremely consistent within an array of thicker catalysts but this consistency decreases for thin catalysts, indicating that

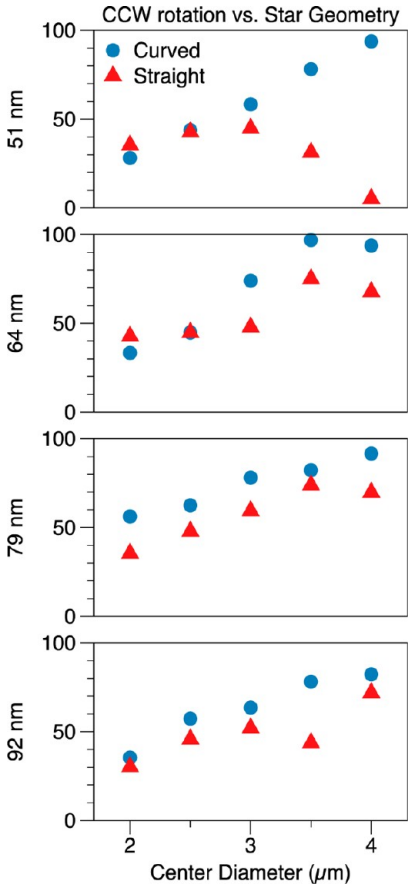

Figure 3. Graph showing the percent CCW rotation as a function of the arm shape, center core diameter, and catalyst thickness. Notice that the curved arms show improved performance over straight arms and that a larger center core diameter also shows better control over rotation direction.

thinner catalysts are more sensitive to small differences in any localized etching conditions.

Higher magnification micrographs of these structures in Figure 5 show the change in deformation mode as the catalyst thickens. Thin catalysts bend with 4-fold symmetry in a manner that preserves the overall star-shape with symmetric protrusion, while thicker catalysts transition to a 2-fold symmetry in which half the catalyst arms are no longer in plane with the central core structure and will have a reduce moment-arm with respect to the rotation axis. The difference in thickness between the 51 nm thick catalyst and 64 nm thick catalyst shown in Figure 5a,b causes only a slight difference in deformation, as evidenced by the minor difference shadowing and buckling seen between the catalysts. As the catalyst thickness increases, the deformation mode transitions to the 2-fold symmetry exemplified by the 79 and 92 nm thick catalysts in Figure 5c,d. This transition marks the start of poor control over catalyst rotation direction as the 2-fold deformation mode shows poorer consistency across each sample array.

The number of arms on the catalyst also plays a role establishing rotation direction. The percentage of CCW rotation *versus* the number of arms for each catalyst thickness for the four different thicknesses is summarized in Figure 6 with representative SEM micrographs found in Supporting Information, Figure S1. For this figure, the number of arms was varied from one to seven with the center core diameter and arm length kept constant at 4 and 2 μm, respectively. It is important to note that catalyst with less than 25% CCW rotations were structures that exhibited largely straight vertical etching with little to no rotation at all. The graphs in Figure 6 clearly illustrate the influence that catalyst geometry plays in determining rotation direction with three and four-arm catalyst thicknesses maintaining the correct geometric configuration necessary for consistent CCW rotation. Examination of the SEM micrographs in Supporting Information, Figure S1 shows that catalysts with more than three to five arms either fold into a ball shape for thinner 51 and 64 nm thick catalysts or bend in half for the thicker 79 and 92 nm thick catalysts. A key outlier is the two-arm, 92 nm thick catalyst which is the only two-arm catalyst that undergoes rotation to any degree. Examining the SEM images shows that this catalyst thickness results in only a little deformation while all the other thicknesses quickly produce bending in half or have their arms bend at the root. These results reinforce the hypothesis that catalyst deformation in the early stages of the etching process plays an important role in establishing rotation direction. Unfortunately, the root cause of this dependency cannot be clearly understood at this time until physical/mathematical models are developed that simulate etching dynamics, material removal, catalyst deformation, and surface−surface interactions in a manner that properly replicates experimental results.

Certain catalyst geometries are not conducive to establishing or maintaining rotation. As noted in Figure 6 and Supporting Information, Figure S1, the one-arm catalyst lacks the protrusions necessary to induce rotation while the thinner catalysts undergo extensive deformation, collapsing into a ball shape that cannot transfer torque about the vertical axis. However, control over rotation direction is maintained for three- and four-arm catalysts even when they are very thin. Higher magnification SEM micrographs of the three- and four-arm catalysts are supplied as Supporting Information, Figure S2 to better illustrate the deformation mode of these structures. It is clear that this geometry maintains excellent control over rotation direction due to the fact that the deformation mode largely maintains the overall protrusion geometry necessary to properly induce torque for rotation. There is also a marked transition in the deformation symmetry at 79 nm thick catalyst. The deformation symmetry of thinner catalysts maintains the symmetry of the original catalyst while thicker catalysts exhibit 2-fold symmetry that is largely independent of catalyst shape,

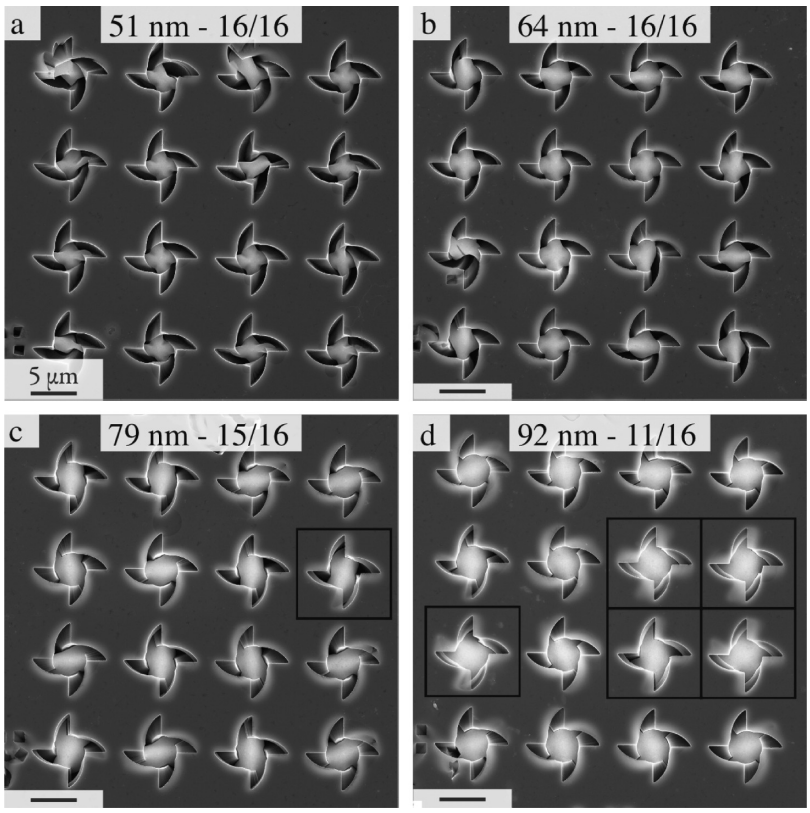

Figure 4. SEM micrographs of catalyst star arrays with the same geometry but with different thicknesses of 51, 64, 79, and 92 nm. For these structures the center diameter was 4 μm, arm length was 2.25 μm, and all catalysts had four arms. The ratio of CCW rotation *versus* the total number of catalysts is given, and the top and any CW rotations are boxed in black. Notice that the ratio of CCW rotation decreases with increasing catalyst thickness. All scale bars are 5 μm as designated in panel a.

which would reduce the ability to control the direction of rotation from catalyst shape alone.

From the graphs in Figure 6 one can conclude that catalyst thickness and the number of arms play an important role in establishing rotation direction. However, it is important to also examine the role of center core diameter and arm length. The graphs in Figure 7 plot the percent CCW rotation for 4 $\times$ 4 arrays of curved and straight-arm catalysts. The center core diameter was varied from 2.0 to 4.0 μm with 0.5 μm increments while the arm length was set to 1.5 or 2.25 μm. As with earlier trends, this data show that the controllability of rotation direction also improves with increasing center core diameter for curved catalyst arms while straight catalyst arms show a sharp decrease in controllability at 4.0 μm. This decrease is attributed to deformation mode problem seen with straight-arm catalysts in which the arm itself bends at the root instead of the entire catalyst structure deforming. We suspect that this difference in deformation mode, that is, bending of the arm *versus* buckling of the entire catalyst structure, is largely responsible for the differences in etching behavior seen between the straight *versus* curved-arm catalysts.

Rotation Angle. As recently detailed and exampled in Figure 8, MaCE is an excellent tool to fabricate templates for electroless deposition of metals. Beyond fabricating arrays of 3D metallic structures, electroless deposition enables us to examine the entire etching path of the catalyst structures to determine the relationship between rotation angle and catalyst geometry. SEM micrographs with the sample tilted at 45° show that the etch depth was 2 $\pm$ 0.2 μm for an etch rate of 6.7 nm/sec and was largely independent of center core diameter, number of arms, or arm length. This result fits the 7 nm/sec etch rate based upon the model developed by Rykaczewski *et al.*[18]

Angle measurements were taken from 9600 Pd structures fabricated using a 92 nm thick catalyst with core diameters ranging from 2.0 to 4.0 μm. The arm lengths were varied as 1.5 or 2.25 μm while the number of arms was varied from three to five. Histograms of the raw and absolute values are provided in the Supporting Information (Figures S3 and S4). As expected the 92 nm thick catalyst shows a bimodal distribution in rotation angle with larger (*i.e.*, core and arm length) catalysts showing more control over rotation direction. The graphs in Figure 9 plot the median absolute rotation angle *versus* center core diameter for three arms (red circle), four arms (blue triangle), and five arms (green square). The top and bottom rows separate results for the straight *versus* curved arms while the left and right columns separate results for the 1.5 and 2.25 μm arm lengths. A linear fit was applied to each set

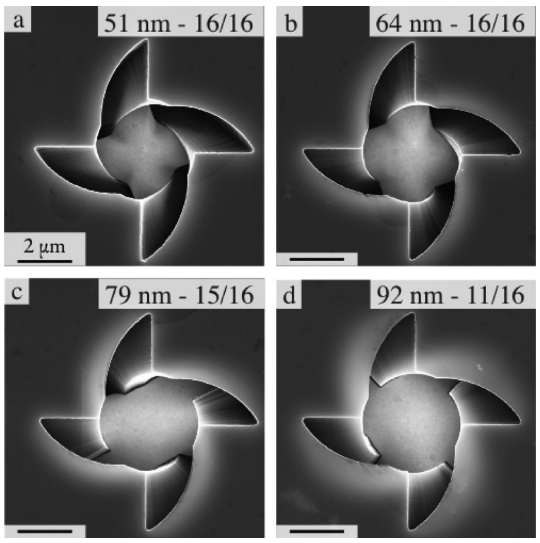

Figure 5. SEM micrographs showing the difference in catalyst deformation with thickness for catalysts of same geometry but with different thicknesses of 51 nm, 64 nm, 79 nm, and 92 nm. For these structures the center diameter was 4 μm, arm length was 2.25 μm, and all catalysts had four arms. (a) The 51 nm thick catalyst bends with 4-fold symmetry; (b) the 64 nm catalyst bends with 4-fold symmetry but the deformation is reduced as evidenced by the lower amount of shadowing in the deformed region; (c) the 79 nm catalyst transitions to bending with 2-fold symmetry and starts to show reduced rotation constancy; (d) 92 nm catalyst bends with 2-fold symmetry and shows even less catalyst deformation as evidenced by the visibility of the deformation side arms. All scale bars are set to 2 μm as designated in panel a.

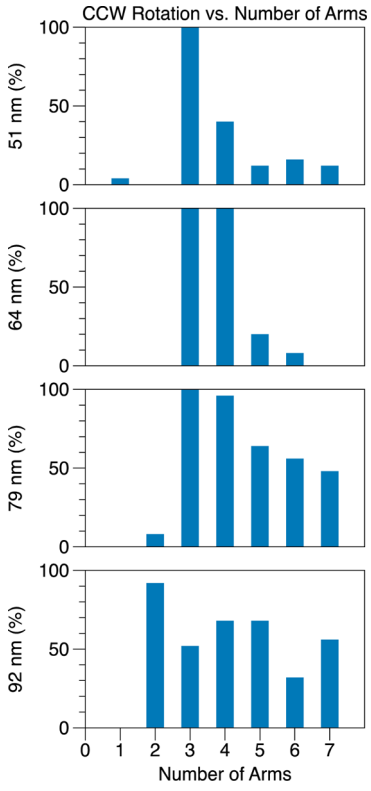

Figure 6. Graph showing the percentage of CCW rotation as a function of the number of arms and the catalyst thickness. Notice that 2 arms is the minimum number to induce rotation and that three or four arms gives the best results across the widest number of catalyst thicknesses. Note that catalysts with less than 25% CCW rotation were catalyst structures that exhibited purely vertical etching with little to no rotation at all.

of arm data as listed in the bottom left corner of each graph (and Table S1 of the Supporting Information) and the error bars are set at the 2 sigma value. From this data it is clear that the rotation angle decreases linearly with increasing core diameter and with relatively consistent slopes and intercepts for all but the three-arm catalysts (of which only three catalysts properly etched). Also, there is a marked decrease in the width of the error bars as the center core diameter increases, indicating that it is easier to control the rotation angle of large diameter catalysts. There also appears to be some change in slope as the arm length varies; however, no trends can be established as only two arm lengths were tested. Future tests will examine the relationship between the number of arms and rotation angle in greater detail.

The etching path can change as the catalyst etches into the sample. For example, the Pd structures fabricated from the 92 nm thick MaCE template show that greater than 90% of the catalysts that rotated in the "wrong" direction, CW, switched directions after ~500 nm of vertical travel. This reinforces the hypothesis that the shape of the catalyst plays a large role in determining etching direction and that the catalyst can deform in a manner that emphasizes CCW rotation. This also reinforces the hypothesis that the shape of the catalyst as it just starts etching influences the etching path and can control the chirality of the etched structure.

Another interesting trend is that the spiraling process often stops after a single 360° rotation or ~1 μm of vertical etching for catalysts with large center core diameters. The top-down images of the etch structure could only discern the initial rotation and rarely revealed the halting of this rotation. Unfortunately, the root cause for this transition from spiraling to vertical etching cannot be determined solely from this study due to the complexity of MaCE. Potential causes could be as simple as excessive catalyst deformation, which would reduce the catalysts ability to properly rotate, or more complex processes could be occurring with a change in the etching kinetics as the catalyst travels into the silicon substrate. Changes in product and reactant concentrations as a function of etch depth and etching time, and gas trapping/evolution during the process could also be a source for the observed changes in etching path.

At this point, a set of basic geometric parameters have been established that can be used for those interested in fabricating 3D spiraling structures with controlled chirality. Specifically, three and four-arm catalysts with curved, sawtooth shaped arms exhibit

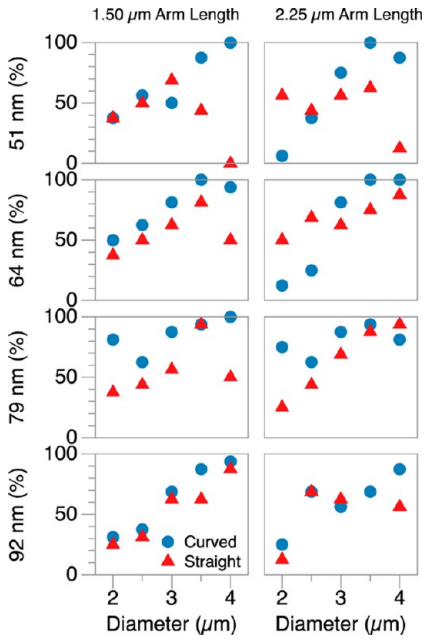

Figure 7. Graphs showing the percentage of CCW rotation as a function of the center core diameter, arm length, and catalyst arm shape for 51, 64, 79, and 92 nm thick catalysts with four arms. Notice that the curved arms typically perform better than straight arms and that the larger center core diameter improves the stability of the catalysts. The effect of difference in arm length is relatively minor.

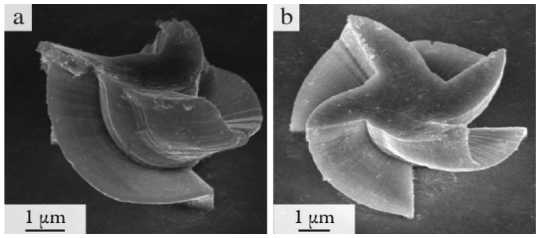

Figure 8. SEM micrographs of 3D spiraling metallic structures fabricated by electroless deposition of Pd into MaCE fabricated Si templates. These micrographs establish the rotation angle and etching path over the entire etch depth.

a highly controlled rotation over a wide range of center core diameters and catalysts thicknesses. Also, the rotation angle when the etch halts can be established within a reasonably narrow range by selecting the correct center core diameter.

While an increasing amount of work has been conducted on the topic of MaCE, considerably more work is needed on the theoretical and modeling front before MaCE will be ready for industrial applications. Specifically, little is known about the etching dynamics of MaCE. It is expected that etchant composition and dilution will change not only if and how much SiO_2 is generated beneath the catalyst, but also the dissolution rate of hole (h^+) rich Si* and/or SiO_2 below the catalyst. Other key unknown parameters are the thickness of the Si*/SiO_2 regions, dissolution rate of these regions as catalyst width increases, and space between the catalyst and the substrate along with how this distance combined with driving forces translates to catalyst motion and deformation. While our group is actively pursuing these questions, it is worth highlighting procedures by Huang *et al*. and Oh *et al*. that use external fields to decouple some of the MaCE processes of Si oxidation and catalyst motion.[30,31] These procedures, wisely applied, should go a long way toward establishing the fundamental dynamics and mechanics to MaCE.

CONCLUSIONS

The results of the comprehensive parametric study presented in this work are intended as a guide for those seeking to develop 3D chiral structures in silicon using MaCE. The catalyst structures exhibiting the highest degree of control of the rotation direction and halting angle were four-arm catalysts with center diameters between 3.0 and 3.5 μm and arm lengths on the order of 1.0−2.25 μm. We show that catalyst deformation plays an important role in establishing rotation direction and structures that deform in manners that preserve the overall shape of the catalyst during the etch allow for the greatest control of resulting chirality. Specifically, above 90% of thin catalysts with three or four arms deform with 3-fold and 4-fold arm bending and rotate counter-clockwise. Catalysts with a large number of arms or those that were excessively thick undergo simple 2-fold arm bending, but still yield robust control over rotation during the etch. Also, curved catalyst arms were found to induce buckling in a manner that preserves the catalyst shape and does not substantially affect the rotation pattern, while straight arms merely bend at the junction between the arms and the core of the star with resulting reduction of the torque that drives the rotational motion. Electroless deposition of Pd into the MaCE-formed templates allowed us to examine the full etch path of the catalysts, yielding a linear relationship between center core diameter and final rotation angle. Overall, this work serves as both a guide for 3D chiral structure fabrication and comprehensive benchmark data set for evaluating the accuracy of future mathematical models on the dynamics of MaCE.

EXPERIMENTAL SECTION

All procedures except for etching, scanning electron microscopy (SEM) imaging and atomic force microscopy (AFM) measurements were conducted in a class 10 or 100 cleanroom environment; all silicon wafers were handled only in the cleanroom prior to catalyst patterning.

All samples were prepared on p-type, 1−5 Ω-cm (100) silicon purchased from UltraSil. First, 350 ± 15 nm, as measured by a

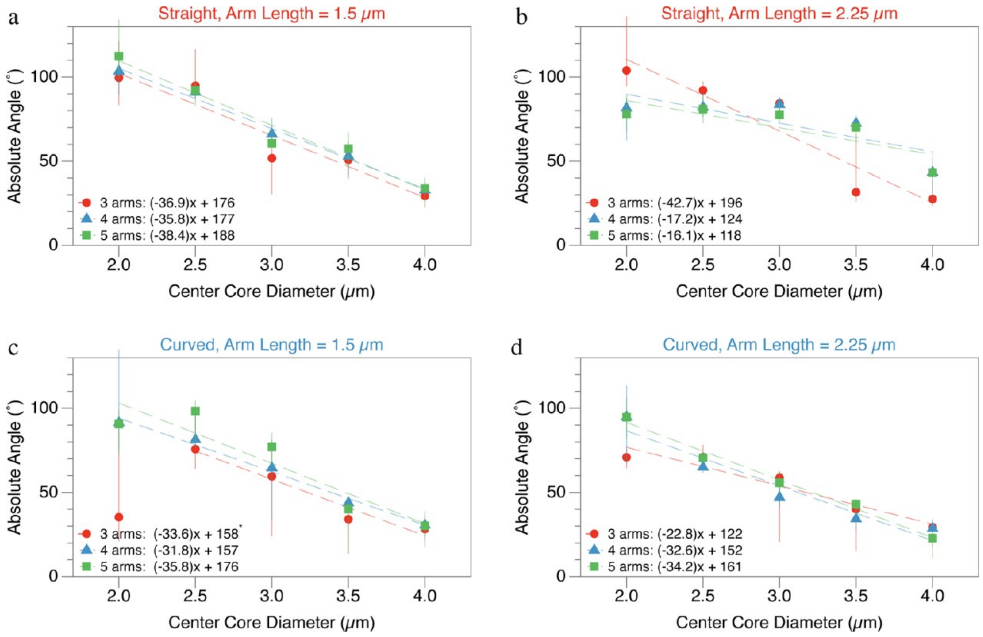

Figure 9. Graphs of median absolute rotation angle as a function of center core diameter for three-arm (red circles), four-arm (blue triangles), and five-arm (green squares) catalysts. The top row shows the results for straight-arm catalysts while the bottom row is for curved-arm catalysts. The columns are separated by arm lengths: 1.50 μm (left) and 2.25 μm (right). A linear fit of median rotation angle *versus* center core diameter for each set of arms is given in the bottom left corner of the graphs. Notice that the slopes and intercepts are relatively consistent within each graph except for the three-arm catalysts, which show more erratic etching. Note: the 2.0 μm diameter, three-arm catalyst was removed from the fit in graph c because only three catalysts actually etched.

Nanospect reflectometer, of polymethyl methacrylate (PMMA) (MicroChem, PMMA-A6) positive resist was spun onto the silicon wafer and baked for 90 s at 180 °C. The PMMA was exposed using a JEOL JBX-9300FS at 100 kV accelerating voltage at 2 nA beam current with a base dose of 680 μC/cm^2 and developed for 120 s in a 1:1 by volume mixture of methyl isobutyl ketone (MIBK)/isopropyl alcohol (IPA) followed by a 120 s rinse in IPA. A 20 nm portion of PMMA was removed use a descum procedure in a PlasmaTherm RIE SLR using O_2 with Ar carrier gas for 30 s at 20 W. The thickness of the catalyst stack was measured using an AFM. Metal lift-off consisted of a 24 h immersion in (Mircoposit 1165 resist remover) at 80 °C as measured using a mercury thermometer. The substrate was cleaned using AMI (sequential acetone, methanol, IPA rinse) and then dried using N_2 (Airgas, 99.99%). Lastly, the samples were descummed in the PlasmaTherm RIE SLR for 60 s under the same conditions as earlier.

Etching. Samples were removed from the cleanroom and MaCE was conducted in the dark using a stagnant $\rho = 90$[13,8] etchant solution of HF:H_2O_2: H_2O = 4:1.3:2.8 mL (Aldrich, 48 wt %: Aldrich, 35 wt %: 15.5 MΩ DI water) carefully applied to the sample to ensure that the etchant solution flowed slowly over the silicon wafer during application. The etchant solution was kept stagnant during etching and the only opportunities for external excitation were when the etchant was applied or removed from the sample. Once etching was complete the sample was immersed for 5 min in ample DI water maintained at room temperature (27 °C) to halt the etching process and then dried using N_2 gas.

Electroless Filling. After etching, the samples were cleaned using a PlasmaTherm RIE SLR O_2 plasma for 8.5 min at 100 W. Next, the samples were transferred in an N_2 filled zip-lock bag back to the cleanroom where electroless Pd was deposited using the Pd-Tech (purchased from Atotech) Pd electroless plating solution. The sample was first placed for 4 min in a predip activating bath of Pd-Tech Activator Additive and deionized water (8%:92% vol) held at 30 °C. The samples were then transferred and immersed for 4 min in a mixture of Pd-Tech Activator Additive/Pd Tech A Concentrated/DI water (8%:6%:86% vol). Next the sample was rinsed with DI water for 1 min and then immersed for 1−1.25 h in a Pd-Tech PC bath of Pd-Tech PC Reducer Solution/Pd-Tech Makeup Solution/DI water (15%:10%:75% vol) and then rinsed for 1 min in DI water and dried under N_2 gas. The expected Pd deposition rate was 3 μm/hour and 4 μm deep templates were properly filled with a slight amount of overfill after 1.25 h.

Template Removal. A thin layer of Au was deposited *via* e-beam evaporation. For the first sample a 5 nm thick adhesion layer of Pd was deposited at 1 Å/s followed by a 500 nm thick layer of Au deposited at 3 Å/s. For the second sample a 5 nm thick layer adhesion layer of Ti was deposited at 1 Å/s followed by a 500 nm thick layer of Au deposited at 3 Å/s. The sample was then immersed in a 25 wt % solution of tetramethyl ammonium hydroxide (TMAH) TMAH/DI water at 80 °C bath temperature as measured using a mercury thermometer.

Observations. All samples were imaged using the In-Lens and SE2 detectors of a Zeiss LEO 1550 thermally assisted field emission (TFE) scanning electron microscope (SEM) operating at 10 kV accelerating voltage and 3−4 mm working distance. The thickness of the catalyst stack was measured using a Bruker Dimension Edge SPM in tapping mode.

Conflict of Interest: The authors declare no competing financial interest.

Supporting Information Available: Detailed experimental procedures and additional figures illustrating how the shape and catalyst thickness change the deformation mode along with how this change in deformation impacts our ability to control catalyst rotation direction; 3D metallic structures fabricated using electroless deposition of Pd into the Si templates fabricated using metal-assisted chemical etching (MaCE); histograms on the rotation angles and absolute rotation angles measured from these 3D metallic structures. This material is available free of charge *via* the Internet at http://pubs.acs.org.

Acknowledgment. O.J.H. and C.P.W. acknowledge financial support of this work through NSF CMMI Grant 113876. A.G.F. was supported by AFOSR BIONIC Center Award No. FA9559-0901-0162. Any opinions, findings, and conclusions or recommendations expressed in this publication are those of the authors and do not necessarily reflect the views of the National Science Foundation.

REFERENCES AND NOTES

1. Gansel, J.; Thiel, M.; Rill, M.; Decker, M. Gold Helix Photonic Metamaterial as Broadband Circular Polarizer. *Science* **2009**, *325*, 1513–1515.
2. Thiel, M.; Rill, M. S.; von Freymann, G.; Wegener, M. Three-Dimensional Bi-chiral Photonic Crystals. *Adv. Mater.* **2009**, *21*, 4680–4682.
3. Weiss, S. M.; Haurylau, M.; Fauchet, P. M. Tunable Photonic Bandgap Structures for Optical Interconnects. *Opt. Mater.* **2005**, *27*, 740–744.
4. Yamada, K.; Fukuda, H.; Tsuchizawa, T. All-Optical Efficient Wavelength Conversion Using Silicon Photonic Wire Waveguide. *IEEE Photonics Technol. Lett.* **2006**, *18*, 1046–1048.
5. Brueck, S. R. J. Optical and Interferometric Lithography-Nanotechnology Enablers. *Proc. IEEE, New York* **2005**, *93*, 1704–1721.
6. Ito, T.; Yamada, T.; Inao, Y.; Yamaguchi, T.; Mizutani, N. Fabrication of Half-Pitch 32 nm Resist Patterns Using Near-Field Lithography with a-Si Mask. *Appl. Phys. Lett.* **2006**, *90*, 1–3.
7. Koynov, S.; Brandt, M.; Stutzmann, M. Black Nonreflecting Silicon Surfaces for Solar Cells. *Appl. Phys. Lett.* **2006**, *88*, 203107-1–203107-3.
8. Kovacs, G. T. A.; Maluf, N. I.; Petersen, K. E. Bulk Micromachining of Silicon. *Proc. IEEE* **1998**, *86*, 1536–1551.
9. M. Gad-el-Hak. *Mems: Applications*; 1st ed.; CRC Press: Boca Raton, FL, 2006.
10. Matsumoto, Y.; Setomoto, M.; Noda, D.; Hattori, T. Cylindrical Coils Created with 3D X-ray Lithography and Metallization. *Microsyst. Technol., Micro-Nanosyst. Inf. Stor. Process. Syst.* **2008**, *14*, 1373–1379.
11. Romanato, F.; Tormen, M.; Businaro, L.; Vaccari, L.; Stomeo, T.; Passaseo, A.; Di Fabrizio, E. X-ray Lithography for 3D Microfluidic Applications. *Microelectron. Eng.* **2004**, *73*, 870–875.
12. Tormen, M.; Businaro, L.; Altissimo, M.; Romanato, F.; Cabrini, S.; Perennes, F.; Proietti, R.; Sun, H. B.; Kawata, S.; Di Fabrizio, E. 3D Patterning by Means of Nanoimprinting, X-ray and Two-Photon Lithography. *Microelectron. Eng.* **2004**, *73*, 535–541.
13. Formanek, F.; Takeyasu, N.; Tanaka, T.; Chiyoda, K. Three-Dimensional Fabrication of Metallic Nanostructures over Large Areas by Two-Photon Polymerization. *Opt. Express* **2006**, *14*, 800–809.
14. Thiel, M.; Decker, M.; Deubel, M.; Wegener, M.; Linden, S.; von Freymann, G. Polarization Stop Bands in Chiral Polymeric Three-Dimensional Photonic Crystals. *Adv. Mater.* **2007**, *19*, 207–210.
15. Leong, T. G.; Zarafshar, A. M.; Gracias, D. H. Three Dimensional Fabrication at Small Size Scales. *Small* **2010**, *6*, 792–806.
16. Hildreth, O.; Wong, C. P.; Xiu, Y. Wet Chemical Method to Etch Sophisticated Nanostructures into Silicon Wafers Using Sub-25nm Feature Sizes and High Aspect Ratios. *Electron. Compon. Technol. Conf., San Diego* **2009**, 860–864.
17. Hildreth, O.; Brown, D.; Wong, C. P. 3d Out-of-Plane Rotational Etching with Pinned Catalysts in Metal-Assisted Chemical Etching of Silicon. *Adv. Funct. Mater.* **2011**, *21*, 3119–3128.
18. Rykaczewski, K.; Hildreth, O.; Wong, C. P.; Fedorov, A.; Scott, J. H. J. Guided Three-Dimensional Catalyst Folding During Metal-Assisted Chemical Etching of Silicon. *Nano Lett.* **2011**, *11*, 2369–2374.
19. Hildreth, O.; Lin, W.; Wong, C. P. Effect of Catalyst Shape and Etchant Composition on Etching Direction in Metal-Assisted Chemical Etching of Silicon to Fabricate 3D Nanostructures. *ACS Nano* **2009**, *3*, 4033–4042.
20. Chun, I. S.; Chow, E. K.; Li, X. 3D Nanoscale Pattern Formation in Porous Silicon. *Lasers Electro-Opt.* **2008**, *76*, 1084–1093.
21. Hildreth, O.; Rykaczewski, K.; Fedorov, A.; Wong, C. P. Controlling the Out-of-Plane Rotation Angle in Metal-Assisted Chemical Etching of Silicon. Submitted for review.
22. Chen, H.; Wang, H.; Zhang, X.; Lee, C.; Lee, S. Wafer-Scale Synthesis of Single-Crystal Zigzag Silicon Nanowire Arrays with Controlled Turning Angles. *Nano Lett.* **2010**, *10*, 864–868.
23. Chartier, C.; Bastide, S.; Lévy-Clément, C. Metal-Assisted Chemical Etching of Silicon in Hf–H_2O_2. *Electrochim. Acta* **2008**, *53*, 5509–5516.
24. Chattopadhyay, S.; Bohn, P. W. Direct-Write Patterning of Microstructured Porous Silicon Arrays by Focused-Ion-Beam Pt Deposition and Metal-Assisted Electroless Etching. *J. Appl. Phys.* **2004**, *96*, 6888–6894.
25. Chattopadhyay, S.; Li, X.; Bohn, P. W. In-Plane Control of Morphology and Tunable Photoluminescence in Porous Silicon Produced by Metal-Assisted Electroless Chemical Etching. *J. Appl. Phys.* **2002**, *91*, 6134–6140.
26. Li, X.; Bohn, P. W. Metal-Assisted Chemical Etching in HF/H_2O_2 Produces Porous Silicon. *Appl. Phys. Lett.* **2000**, *77*, 2572–2574.
27. Huang, Z.; Geyer, N.; Werner, P.; Boor, J. d.; Gösele, U. Metal-Assisted Chemical Etching of Silicon: A Review. *Adv. Mater.* **2010**, 285–308.
28. Li, X. Metal Assisted Chemical Etching for High Aspect Ratio Nanostructures: A Review of Characteristics and Applications in Photovoltaics. *Curr. Opin. Solid State Mater. Sci.* **2011**, *16*, 71–81.
29. Rykaczewski, K.; Hildreth, O.; Wong, C. P.; Fedorov, A. Directed 2D–3D Pattern Tranfer Method for Controlled Fabrication of Topologically Complex Three-Dimensional Features in Silicon. *Adv. Mater.* **2010**, *23*, 659–663.
30. Oh, Y.; Choi, C.; Hong, D.; Kong, S. D.; Jin, S. Magnetically Guided Nano–Micro Shaping and Slicing of Silicon. *Nano Lett.* **2012**, *12*, 2045–2050.
31. Huang, Z. P.; Geyer, N.; Liu, L. F.; Li, M. Y.; Zhong, P. Metal-Assisted Electrochemical Etching of Silicon. *Nanotechnology* **2010**, *21*, 1–6.